

Characterisation and fluid transport simulations of fractures and fracture networks

Autor: Prof. Dr. habil. Heinz Konietzky & Dr. rer. nat. Conny Zeeb (TU Bergakademie Freiberg, Geotechnical Institute)

Abbreviations	3
Nomenclature	3
1 Introduction.....	6
2 Properties characterizing fractures and fracture networks.....	8
2.1 Properties of individual fractures	8
2.1.1 Fracture wall rock rheology	8
2.1.2 Fracture geometry.....	9
2.1.3 Fracture filling	10
2.2 Properties of fracture networks.....	11
2.2.1 Fracture density	12
2.2.2 Fracture intensity	12
2.2.3 Fracture spacing	12
2.2.4 Fracture mean length and length distribution	12
3 Difficulties and biases associated with fracture sampling.....	15
3.1 Common sampling difficulties	15
3.2 Sampling biases	16
3.2.1 Orientation bias.....	16
3.2.2 Truncation bias	16
3.2.3 Size bias	17
3.2.4 Censoring bias	18
4 Sampling methods.....	18
4.1 Scanline sampling method	19
4.2 Window sampling method	20
4.3 Circular estimator method	20
5 Modeling of fracture networks	21
6 Fluid transport simulations.....	24
6.1 Fluid transport through a single fracture	24
6.1.1 Spatial distribution of fluid flow.....	24
6.1.2 Cubic law assumption	25

6.2	Fluid transport through a fracture network.....	26
6.2.1	Hydraulic properties of a DFN.....	26
6.2.2	Equivalent porous media	28
6.2.3	Representative elementary volume.....	28
7	References	29

Abbreviations

1D	One dimensional
2D	Two dimensional
3D	Three dimensional
CE	Circular estimator
cdf	Cumulative distribution function
DEM	Discrete element method
DFN	Discrete fracture network
EPM	Equivalent porous media
FEM	Finite element method
FDM	Finite difference method
pdf	Probability density function
Q	Quality index
REV	Representative elementary volume
RMR	Rock mass rating
RQD	Rock quality designation
SLS	Scanline sampling
WS	Window sampling

Nomenclature

a_h	Hydraulic fracture aperture [m]
a_m	Mechanical fracture aperture [m]
A	Area of a sampling window [m ²]
d	Distance between a data point and a line for the evaluation of a lower cut-off length in a log-log plot of fracture length against fracture frequency [-]
E	Exponent of a power-law equation [-]
E_{1D}	Exponent of power-law distributed fracture lengths measured by scanline sampling [-]
E_{2D}	Exponent of power-law distributed fracture lengths measured by window sampling [-]
E_{3D}	Exponent of power-law distributed fracture sizes in a rock volume [-]
g	Gravitational acceleration [m s ⁻²]
h	Hydraulic head [m]
l	Fracture intensity:
P_{10}	Linear fracture intensity [1 m ⁻¹]
P_{21}	Areal fracture intensity [m m ⁻²]
P_{32}	Volumetric fracture intensity [m ² m ⁻³]
j	Designator for individual fracture sets [-]
JCS	Joint compressive strength [Pa]
JRC	Joint roughness coefficient [-]

k	Hydraulic conductivity [m s^{-1}]
k_{\max}	Maximum hydraulic conductivity [m s^{-1}]
k_{\min}	Minimum hydraulic conductivity [m s^{-1}]
k_{xx}	Hydraulic conductivity in x-direction [m s^{-1}]
k_{xy}	Hydraulic conductivity in xy-direction [m s^{-1}]
k_{yy}	Hydraulic conductivity in y-direction [m s^{-1}]
K	Permeability [m^2]
l	Fracture trace length [m]
l_0	Lower cut-off length for fracture traces [m]
l_m	Mean fracture trace length [m]
L	Length of a scanline [m]
m	Number of fracture endpoints inside a circular scanline [-]
n	Number intersections between fractures and a circular scanline [-]
N	Total number of sampled fractures [m s^{-1}]
<i>Ocurrence</i>	Frequency of an individual fracture [1 m^{-1}]
ρ	Fracture density:
$P20$	Areal fracture density [1 m^{-2}]
$P30$	Volumetric fracture density [1 m^{-3}]
q_x	Fluid flux in x-direction [$\text{m}^3 \text{ s}^{-1}$]
q_y	Fluid flux in y-direction [$\text{m}^3 \text{ s}^{-1}$]
Q	Fluid flux [$\text{m}^3 \text{ s}^{-1}$]
r	Radius of a circular scanline [m]
S	Fracture spacing [m]
S_{2D}	True fracture spacing between two fracture traces [m]
S_{3D}	True fracture spacing between two fracture planes [m]
S_A	Apparent fracture spacing [m]
UCS	Uniaxial compressive strength [Pa]
v	Fluid velocity [m s^{-1}]
α	Dip direction of a scanline [$^\circ$]
β	Dip of a scanline [$^\circ$]
α_j	Average dip direction of the j -th fracture set [$^\circ$]
β_j	Average dip of the j -th fracture set [$^\circ$]
$\delta h / \delta x$	Gradient of hydraulic head in x-direction [m m^{-1}]
$\delta h / \delta y$	Gradient of hydraulic head in y-direction [m m^{-1}]
θ_{2D}	Angle between the normal of a fracture trace and a scanline [$^\circ$]
θ_{3D}	Angle between the normal of a fracture plane and a scanline [$^\circ$]
μ	Fluid viscosity [Pa s]
Φ	Angle of the hydraulic head gradient [$^\circ$]
Φ_{\max}	Angle of the maximum hydraulic conductivity [$^\circ$]

1 Introduction

Mechanical discontinuities, such as fractures, joints or faults, have a significant impact on the stability and the fluid transport capabilities of a rock mass. The terminology for mechanical discontinuities in rocks is extensive (e. g. Van der Pluijm & Marshak, 2004) and notations often adhere to processes leading to their formation. However, in geology it is common to distinguish between three types of fractures (e. g. Pollard & Segall, 1987; Scholz, 2002; Bons et al., 2012): (1) Extensional fractures with an opening vector perpendicular to the fracture plane; (2) Oblique opening or hybrid fractures with an opening vector at an oblique angle to the fracture plane; (3) Shear fractures without any opening mode component. For convenience the general term “fracture” is used throughout this manuscript.

A variety of properties can be measured and calculated directly or indirectly to characterize individual fractures and fracture networks. To minimize the time required for the characterization only those properties relevant for a specific case study should be evaluated. For example, the stability of a rock mass is commonly described by some kind of quality index, such as the Rock Quality Designation (RQD), the Rock Mass Rating (RMR), or the Quality Index (Q) (e. g. Goel and Singh, 2011). These quality indices are typically evaluated based on a “rudimentary” description of the rock condition (e. g. unweathered or weathered) and the fractures (e. g. fracture spacing) encountered at rock faces. For example, the lining of a tunnel is constantly adapted to the local rock conditions.

Insitu measurements for the simulation of fluid transport through a fractured rock mass are commonly scarce and are limited to highly confined, high-resolution data from boreholes and low-resolution data from seismics. Outcrops of rock masses analogue to those encountered in the subsurface provide an opportunity to evaluate high-resolution data. Such outcrops can extend over several up to hundreds of meters and are therefore less confined than boreholes. However, the obtained data often needs to be extrapolated into the subsurface and/or over large distances. Thus, simulations of fluid transport in fracture networks are commonly treated in a stochastic framework, which requires a more detailed characterization of the studied fractures and fracture networks (Lee & Farmer, 1993; Blum et al., 2005).

This manuscript provides an introduction to the characterization of fracture networks and subsequent fluid transport simulations. The chapters of the manuscript discuss and summarize (1) the properties characterizing fractures and fracture networks, (2) typical difficulties and biases associated with fracture sampling, (3) commonly applied sampling methods, (4) the modeling of fracture networks, and (5) the simulation of fluid transport in a single fracture and in a fracture network.

The importance of fractures and fracture networks

The impact of discontinuities on rock mass stability was studied, for example, by Sellers and Klerck (2000). They showed that the presence of discontinuities around excavations considerably increases the amount of post-excavation fracturing, thereby weakening pillar stability. Moreover, the inflow of water into open cavities can be significantly increased due to the presence of mechanical discontinuities, especially in rocks with negligible permeability (Goel and Singh, 2011).

The contribution of fractures to the overall fluid transport in a rock mass is special importance for the heat extraction from geothermal systems, the exploitation of hy-

hydrocarbon reservoirs, the abstraction of groundwater in fractured aquifers, and the safety of high-risk waste-repositories. For example, Sausse et al. (2010) created a 3D model of the fracture system in the Soultz-sous-forêts geothermal reservoir. This model was generated by extrapolating the fracture data measured in the wells to the whole reservoir. Such models are key to planning and executing the procedure of hydraulic stimulation and a sustainable heat production. Another research study by Belayneh et al. (2009) conducted water flooding simulations based on fracture network data to predict the water breakthrough in a hydrocarbon reservoir. The aim of such simulations is to maximize the production and to minimize the risk of generating a shortcut between the water injection-well and the production well from which the oil/gas is produced. Creating a shortcut might result in the production of water instead of hydrocarbons, thereby rendering the production well useless. Zeeb et al. (2010) studied a fractured rock aquifer situated in the Wajid sandstone formation in Saudi Arabia. Although the studied sandstone exhibits a high permeability their results indicate that the fluid transport in this subsurface aquifer is controlled by the fracture network. The work conducted by Blum et al. (2005) assessed particle travel times from a hypothetical high-risk waste repository near Sellafield (UK) into the biosphere along fault systems and fracture networks. The density and apertures of the fracture network were varied depending on the uncertainty range of measured properties. The particle travel times ranged between a few tens of years for fracture networks with high hydraulic conductivities and several hundred thousand years for fracture networks with low hydraulic conductivities.

The examples presented above illustrate well the importance of assessing the impact of fractures and fracture networks. Neglecting fractures might cause an overestimation of rock mass stability or an underestimation of the overall fluid transport. As a consequence high additional costs might arise due the presence of unexpected discontinuities. In the worst case a project might even fail completely.

2 Properties characterizing fractures and fracture networks

A variety of properties can be measured and calculated (directly or indirectly) to characterize individual fractures and fracture networks. However, it is rarely necessary (or desirable) to measure all possible properties of a fractured rock mass. On the other hand, measuring additional properties later on is not always possible. A well planned field campaign is therefore key to an efficient fracture network characterization. The chapter summarizes commonly used properties used to characterize individual fractures and fracture networks.

2.1 *Properties of individual fractures*

In this section properties used to characterize fractures are described. Common characterizations include descriptions of (1) the fracture wall rock rheology, (2) the fracture geometry, and (3) the fracture filling (e. g. Lee and Farmer, 1993; Barton and Quadros, 1997; Renshaw et al., 2000; Laubach 2003; Laubach and Ward, 2006). A summary of the presented properties is provided in Table 1.

2.1.1 *Fracture wall rock rheology*

Wall rock rheology encompasses the properties of the fracture wall, such as the uniaxial compressive strength (UCS), the joint compressive strength (JCS), and the joint roughness coefficient (JRC). The UCS describes the strength of the fracture wall material to withstand load. The JCS describes the strength of the fracture surface itself and is typically lower than the UCS due to asperities on the fracture surface failing at lower loads. The JRC is a dimensionless value that can be used to describe the roughness (asperities) of a fracture wall (Fig. 1). UCS, JCS, and JRC can be used to model fracture closure under load (Barton & Bandis, 1980; Barton et al., 1985).

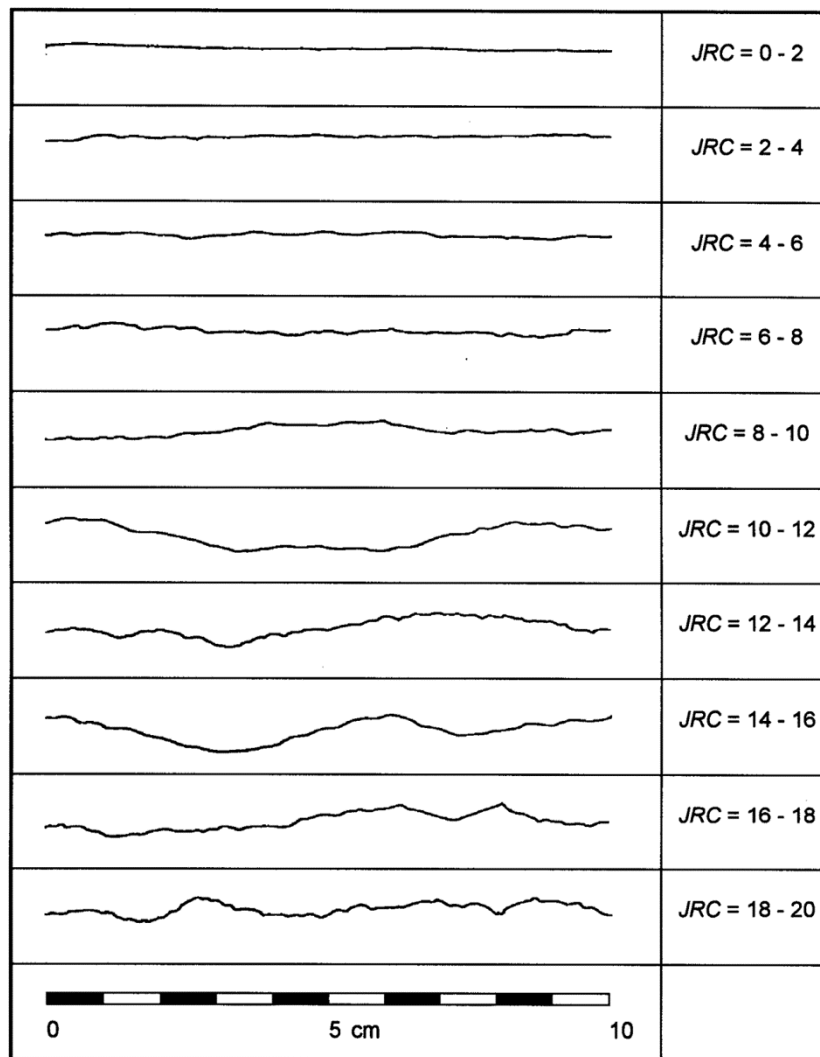


Fig. 1. Roughness profiles and corresponding JRC values (after Barton and Choubey, 1977).

2.1.2 Fracture geometry

The geometric properties of a fracture encompass fracture orientation, size, aperture and displacement. Fracture orientation can be used to reconstruct the palaeo-stressfield, which led to the mechanical failure of the rock thereby creating the observed fractures (e. g. Bons et al., 2012). Moreover, orientation is also often used as an indicator to group fractures into sets, with longer fractures typically following a preferential orientation more closely than shorter ones. The 3D orientation of a fracture is defined by the fracture dip and dip direction, and the 2D orientation by the fracture strike.

For the characterization of fracture aperture it is necessary to distinguish between the mechanical aperture a_m and the hydraulic aperture a_h . The mechanical aperture describes the distance between the two fracture walls. The hydraulic aperture a_h is related to fluid transport simulations applying the cubic law (chapter 6.1.2) and can be thought of as the average aperture of a fracture neglecting the asperities on the fracture surfaces. A relationship between mechanical aperture, joint roughness JRC and hydraulic aperture is presented by (e.g Barton and de Quadros, 1997):

$$a_h = \frac{a_m^2}{JRC^{2.5}} \quad \text{Eq. 1}$$

where a_m and a_h are in microns, and $a_h \leq a_m$.

Fracture size and size distributions (chapter 2.2.4) are important properties for the simulation of fluid transport in fractured rocks (e. g. Philip et al., 2005). Descriptions of fracture size encompass the (1) length of the fracture trace on a rock face (1D), (2) the area of the fracture surface (2D), and (3) the volume of the fracture void (3D). The sampling of fracture sizes can be difficult, especially the measurement of fracture area and volume. Therefore, the trace-lengths of fractures on the surface of outcrops are typically used for fracture size descriptions.

Displacement, also referred to as mismatch length, is a measure of the shear movement parallel to the fracture plane. This displacement of fracture walls and their asperities against each other causes a so-called self-propping of fractures, thereby preserving a residual fracture aperture even under high confining pressures (Durham & Bonner, 1994). Moreover, fracture wall displacement results in a high spatial variation of fracture apertures (Fig. 2). In some places the asperities on the fracture walls touch and the fracture is completely closed, whereas in other parts of the fracture considerable cavities might form. Fluid transport through the fracture is then channeled through interconnected cavities (see section 6.1.1) (e. g. Schwarz & Enzmann, 2013).

2.1.3 Fracture filling

The filling of a fracture controls its mechanical reaction to load and its hydraulic properties. For example, a fracture filled by mineral precipitations (e. g. veins) can withstands higher loads and significantly reduces or even completely inhibits fluid transport.

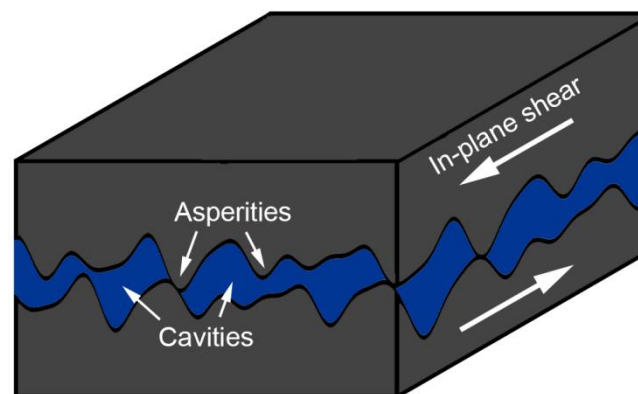


Fig. 2. Sketch of a fracture with rough surfaces. The rock material is highlighted in dark grey and the fracture void in blue. In-plane shear movements cause a displaced fracture walls and the thereby created spatial variation of fracture apertures cause a channeling of fluid transport through interconnected cavities.

Table 1. Properties commonly used to characterize a fracture (modified from Zeeb et al., 2013).

Characteristic	Fracture property	SI unit	Definition
Wall rock rheology	UCS	Pa	Uniaxial compressive strength
	JCS	Pa	Joint compressive strength
	JRC	-	Joint roughness coefficient
Orientation	2D	°	Fracture strike
	3D	°	Fracture dip and dip direction
Size	Length (l)	m	Length of a fracture trace on a surface (e. g. outcrop)
	Area	m ²	Area of the fracture surface
	Volume	m ³	Volume of the fracture void
Geometry	Mechanical (a_m)	m	Distance between two fracture walls
	Aperture	Hydraulic (a_h)	m
Displacement		m	Measure of shear displacement for fracture walls
Filling		-	Description of the material inside the fracture void

Table 2. Summary of fracture network properties commonly used to characterize fracture networks (modified from Zeeb et al., 2013).

Property	SI unit	Definition	
Density (ρ)	Areal ($P20$)	m ⁻² Number of fractures per unit area	
	Volumetric ($P30$)	m ⁻³ Number of fractures per unit volume	
Intensity (I)	Linear ($P10$)	m ⁻¹ Number of fractures per unit length	
	Areal ($P21$)	m m ⁻² Fracture length per unit area	
	Volumetric ($P32$)	m ² m ⁻³ Fracture area per unit volume	
Spacing (S)	m	Average distance between fractures	
Mean length (l_m)	m	Average fracture length	
Length distribution	Scanline sampling	-	Trace length of fractures intersecting with a scanline
	Window sampling	-	Trace length of fractures inside a sampling area

2.2 Properties of fracture networks

This section summarizes the properties commonly used for the characterization of fracture networks: (1) fracture density, (2) fracture intensity, (3) fracture spacing, (4) fracture mean length and (5) fracture length distribution (e. g. Priest, 1993; Neuman, 2008). Table 2 summarizes above properties. Dershowitz (1984) introduced notations to distinguish between areal and volumetric fracture densities ($P20$, $P30$), as well as between linear, areal and volumetric fracture intensities ($P10$, $P21$, $P32$). The sections below describe the presented fracture network properties in detail.

2.2.1 Fracture density

The fracture density p is the number of fractures in a sampling area $P20$ or a sampling volume $P30$. The areal fracture density is typically evaluated for fracture networks on a rock surface applying the window sampling or circular estimator methods (chapters 4.2 and 4.3). Fracture density might be overestimated due to censoring bias (chapter 3.2.4). Therefore, only fractures with the majority of the fractures size, or respectively their fracture center, inside the sampling area should be considered for the calculation of fracture density. However, it can be difficult to decide whether a fracture belongs to a sampling area or not, especially if a fracture cannot be observed over its total length.

2.2.2 Fracture intensity

The fracture intensity I denotes the number of fractures intersecting a line $P10$, the total length of fractures in a sampling area $P21$, or the total area of fracture planes in a rock mass volume $P32$. Linear fracture intensity is also often referred to as fracture frequency and is evaluated applying scanline sampling (chapter 4.1) to borehole data (e. g. cores or image logs) or the surface of outcrops. An areal fracture intensity is typically calculated for fracture networks on rock surfaces, for example by applying the window sampling or circular estimator methods (chapters 4.2 and 4.3). Orientation bias (chapter 3.2.1) causes the calculation of an apparent intensity, thereby underestimating true fracture intensity. Fracture intensities can be estimated from the product of fracture density and fracture mean length.

2.2.3 Fracture spacing

The fracture spacing S is the distance between adjacent fractures along a scanline transecting these fractures and the average spacing of a complete fracture network is equal to $1/P10$. Fracture spacing is evaluated similar to linear fracture intensity by applying the scanline sampling method (chapter 4.1) to borehole data (e. g. cores or image logs) and on the rock surfaces of outcrops. Orientation bias (chapter 3.2.1) causes an overestimation of true fracture spacing.

2.2.4 Fracture mean length and length distribution

Fracture mean length l_m is the average length of all fracture traces measured on the rock surface of an outcrop. The fracture mean length evaluated for power-law distributed fracture lengths should be used with care. Considering the absence of a characteristic scale in power-law functions and the limited information on lower and upper thresholds of fracture lengths in natural systems, a mean value is only valid for the sampled fracture length population. Using such a property, for example for the up-scaling of hydraulic properties, is therefore meaningless (Zeeb et al., 2013).

A more important property for the simulation of fluid transport through a fracture network is the distribution of fracture lengths (e. g. Philip et al., 2005), which describes the probability of a certain fracture length to be part of a fracture length population. Length distributions of natural fracture networks reported in literature are: (1) truncated power-law (e. g. Pickering et al., 1995; Odling 1997; Blum et al., 2005; Tóth, 2010), (2) log-normal (e. g. Priest and Hudson, 1981), and (3) exponential (Cruden, 1977). Several arguments (Bonnet et al., 2001) favor power-law relationships and are therefore the most commonly used to describe the distribution of fracture lengths. An important point is the absence of a characteristic length scale in the fracture growth process. However, all power-law distributions in nature are bound by a lower and up-

per cut-off. The growth of a fracture can be restricted, for example, by lithological layering. The presence of such a characteristic length scale (e. g. the layer thickness) can give rise to log-normal distributions (Bonnet et al., 2001), even though the underlying fracture growth process is a power-law.

Fracture length distributions are typically described as (1) probability density function (pdf) or (2) cumulative distribution function (cdf). A pdf is evaluated by sorting the measured fracture lengths from longest to shortest, calculating their normalized cumulative frequency, and fitting a function to the data. The cdf is evaluated similarly, but fracture lengths are sorted from shortest to longest. Fig. 3 shows the pdf (Fig. 3a) and the cdf (Fig. 3b) of a truncated power-law distribution of fracture lengths.

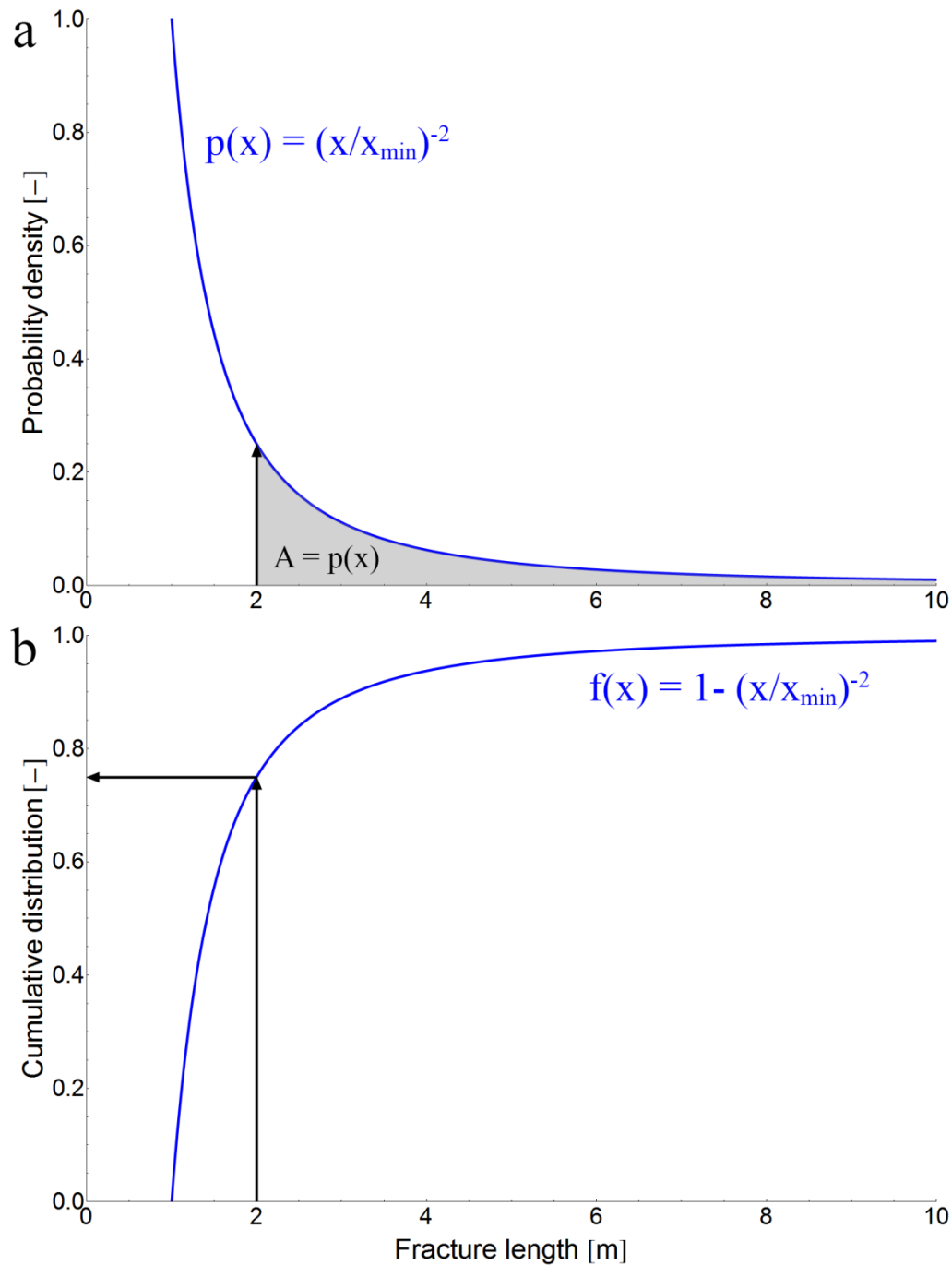


Fig. 3. Plot of fracture lengths with a truncated power-law distribution with a minimum length $x_{\min} = 1$. (a) shows a probability density plot of fracture lengths for a pdf $p(x)$. For a target fracture length of two meters (black arrow) the pdf states that 25 % of the fractures have a length of two meters or more, which corresponds to the area A below the plotted pdf function. (b) shows a cumulative distribution plot of fracture lengths for a cdf $f(x)$. For a target fracture length of two meters (black arrow) the cdf states that 75 % of the fractures have a length of two meters or less, which is indicated by the black arrows.

3 Difficulties and biases associated with fracture sampling

Difficulties and biases associated with fracture sampling can have a significant effect on the evaluation of statistical properties for fracture networks (e. g. Zhang and Einstein, 1998). This chapter describes commonly encountered difficulties, such as (1) fracture sampling from boreholes and (2) the identification of fracture lengths. In addition, a summary of sampling biases and correction techniques is provided for: (1) orientation bias, (2) truncation bias, (3) size bias, and (4) censoring bias.

3.1 Common sampling difficulties

The measurement of fracture properties is not always easy and it is necessary to be aware of possible difficulties. For example, sampling of fractures in the subsurface is generally restricted to well cores or image logs from boreholes. This in-situ information provides valuable data on fracture aperture, spacing, orientation and cementation (e. g. Olson et al., 2009). However, fracture sampling strongly depends on borehole inclination and fracture orientation. Latter significantly reduces potential data for fracture sets parallel to a borehole (e. g. Zeeb et al., 2013). Some properties, such as average fracture spacing (Narr, 1996) and fracture frequency (Ortega and Marrett, 2000) can be estimated irrespectively of borehole inclination.

Fracture size can only be measured indirectly using techniques such as ground penetration radar, electrical resistance tomography and seismics (e. g. Sudha et al., 2011; Forte et al., 2012; Jeanne et al., 2012). The major drawbacks of these techniques are the limitations in penetration depth and resolution. Another possibility to estimate fracture length is the use of scaling relationships between aperture and length for opening-mode fractures (e. g. Olson, 2003; Scholz, 2010). However, the exact nature of these relationships is still under debate (e. g. Olsen & Schultz, 2011) and scaling relationships for fractures in layered rocks have not been systematically investigated yet (e. g. Zeeb et al., 2013). Fracture lengths and their distribution are commonly evaluated analyzing outcropping subsurface analogues. However, the identification of individual fractures can be difficult. For example, a fracture identified

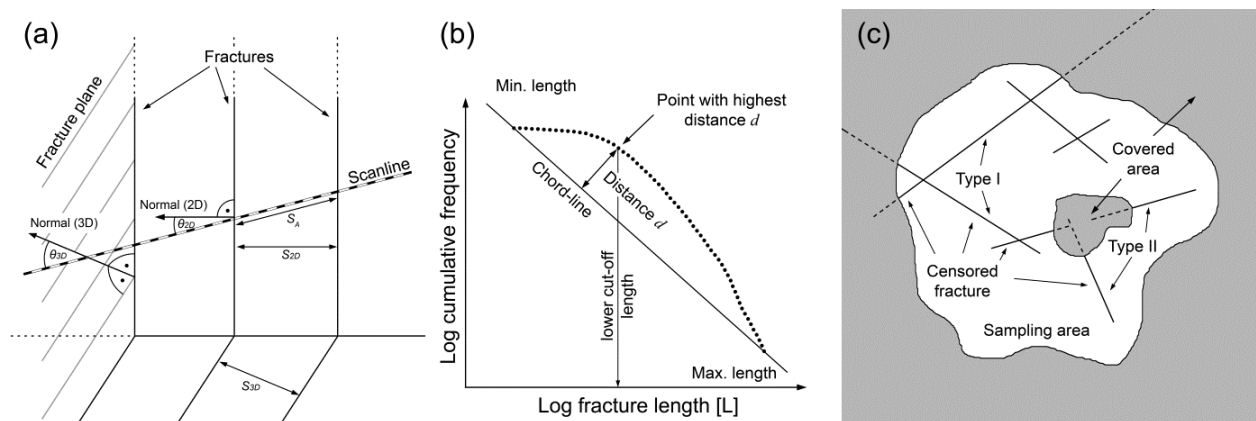


Fig. 4. (a) Sketch illustrating orientation bias and the definition of the variables required for the Terzaghi correction (Eq. 2). S_A is the apparent spacing measured along a scanline, S_{2D} is the true spacing between two fracture traces and S_{3D} is the true spacing between two fracture planes. θ_{2D} and θ_{3D} are the angles between the normal to a fracture trace, or a fracture plane respectively, and a scanline. (b) Illustration of the Chord method (Pérez-Claros et al., 2002; Roy et al., 2007). (c) Censoring bias caused by the boundaries of a sampling area (Type I) and covered parts in an outcrop (Type II) (Zeeb et al., 2013).

as a single strand at one scale of observation (e. g. satellite or aerial image), may be seen as linked segments when changing the scale of observation (e. g. at ground level) (Zeeb et al., 2013). Additional complexity is added by intersecting fractures (e. g. Ortega and Marrett, 2000) and cementation (e. g. Olson et al., 2009; Bons et al., 2012). Thus, an important key factor for fracture network analysis is linking observations made in the subsurface to those obtained from outcrops (e. g. Zeeb et al., 2013).

3.2 Sampling biases

3.2.1 Orientation bias

Orientation bias is associated to fractures intersect an outcrop surface or scanline at oblique angles, which results in the measurement of an apparent spacing S_A between two adjacent fractures. Orientation bias causes an underestimation of linear fracture intensity, or respectively an overestimation of fracture spacing (Fig. 4a). The bias can be reduced or even completely avoided by placing a scanline perpendicular to a fracture set and, if necessary, additional scanlines for different fracture sets. The bias is commonly corrected by applying the Terzaghi correction (Terzaghi, 1965; Priest, 1993):

$$S = S_A \cdot \cos \theta_{2D} \quad \text{Eq. 2}$$

where S is the true spacing and θ_{2D} is the acute angle between the normal to a fracture trace and a scanline. In 3D $\cos \theta_{3D}$ is given by (Hudson and Priest, 1983):

$$\cos \theta_j = \cos(\alpha - \alpha_j) \cos \beta \cos \beta_j + \sin \beta \sin \beta_j \quad \text{Eq. 3}$$

where α and β are the dip direction and dip of the scanline, α_j and β_j the dip direction and dip of the j -th fracture set normal, and θ_j is the angle between the normal to a fracture set plane and a scanline. A drawback of the Terzaghi correction is that fractures need to be grouped into sets. An alternative method for the correction of orientation bias is presented by Lacazette (1991):

$$\text{Occurrence} = \frac{1}{L \cdot \cos \theta} \quad \text{Eq. 4}$$

where *Occurrence* may be thought of as the frequency of an individual fracture, L is the length of a scanline and θ is the angle between the pole to the fracture and the scanline. Applying this method the bias of each individual fracture is corrected and the fracture frequency of a set is the sum of the *Occurrence* values for individual fractures.

3.2.2 Truncation bias

Truncation bias is caused by the unavoidable resolution limitations of a detection device (e. g. satellite image) and a low contrast between the host rock and the studied fractures. As a result, the length or width of a fracture is not detectable below a certain scale. Moreover, as fracture size approaches the detection limit, the actual number of recognized fractures significantly decreases (e. g. Zeeb et al., 2013). Thus, truncation bias is commonly corrected by defining a lower cut-off of fracture size based on data resolution and all fracture sizes below this cut-off are neglected in the

calculation of fracture network properties (Nirex, 1997b). One technique to define the lower cut-off of fracture size is the application of the Chord method (Fig. 4b) (Pérez-Claros et al., 2002; Roy et al., 2007). In a log-log plot of fracture lengths against their cumulative frequency, the line through the data point of the shortest fracture length and the data point of the longest fracture length is calculated. The fracture length from the data point with the highest distance d to this line is used as lower cut-off for the truncation bias (e. g. Zeeb et al., 2013).

3.2.3 Size bias

Size bias is a scanline sampling specific bias (Bonnet et al., 2001). The probability of a fracture to intersect a scanline is proportional to fracture length and therefore shorter fractures are underrepresented in the length data (Fig. 5a) (Priest, 1993; LaPointe, 2002). Hence, the fracture mean length is overestimated and a 1D fracture length distribution is evaluated, which differs significantly from the 2D length distribution. The correction of size bias depends on assumptions of (1) the fracture shape, (2) the spatial distribution of fractures, and (3) the fracture length distribution (e. g. LaPointe, 2002; Darcel et al., 2003; Barthélémy et al., 2009).

A summary of equations and assumption to correct size bias for power-law distributed fracture lengths is presented below. The lengths of fracture traces on a 2D rock face follow a power-law distribution, if fractures are uniformly distributed, disc-shaped and disc-diameters follow a power-law distribution. Based on these assumptions and for well-sampled representative populations fractures Darcel et al. (2003) provide a relationship between three-dimensional (3D), two-dimensional (2D), and one-dimensional (1D) exponents E of a power-law length distribution:

$$E_{3D} = E_{2D} + 1 = E_{1D} + 2 \quad \text{Eq. 5}$$

where E_{3D} is the exponent for a 3D rock mass volume, E_{2D} is the exponent for a 2D sampling area, and E_{1D} is the exponent for a 1D scanline. For non-disc-shaped fractures with strong spatial correlation, clustering, or directional anisotropy, Hatton et al. (1993) provide a more appropriate relationship between 3D and 2D exponents:

$$E_{3D} = A \cdot E_{2D} + B \quad \text{Eq. 6}$$

where $A = 1.28 \pm 0.30$ and $B = -0.23 \pm 0.36$. However, to correlate the 1D and 2D power-law exponents of length distributions Eq. 5 needs to be applied. The mean length l_m of power-law distributed fracture lengths with an exponent E_{2D} can be calculated for a given minimum fracture length l_0 by (LaPoint, 2002):

$$l_m = \frac{E_{2D} l_0}{E_{2D} - 1} \quad \text{Eq. 7}$$

Combination of Eq. 5 and Eq. 7 allows the calculation of an unbiased mean length (Zeeb et al., 2013):

$$l_m = \frac{(E_{1D} + 1) l_0}{E_{1D}} \quad \text{Eq. 8}$$

3.2.4 Censoring bias

A fracture is called censored, if the total fracture length is not observable. Censoring bias can be caused either by (1) the limited outcrop size (Type I: Fractures with one or both ends outside the sampling area), or (2) by uneven outcrop surfaces (e. g. erosion features) and coverage by overlaying rock layers or vegetation (Type II: Fractures with both ends inside the sampling area, but partly hidden from observation) (Fig. 4c) (Priest, 1993; Pickering et al., 1995; Bonnet et al., 2001; Zeeb et al., 2013). A typical effect of censoring bias is an overestimation of fracture density (e. g. Kulatilake and Wu, 1984; Mauldon et al., 2001). Moreover, the uncertainty of calculated fracture network properties increases with the percentage of censored fractures (Zeeb et al., 2013). Correction techniques and equations for censoring bias rely on assumptions of (1) fracture shape (e. g. disc, ellipsoid or rectangle), (2) size distribution (Priest, 2004), and (3) spatial distribution (Riley, 2005). Presenting all of the techniques and equations for different assumptions is beyond the scope of this manuscript.

4 Sampling methods

This section presents three commonly used sampling methods (Fig. 5): (1) the scanline sampling, (2) the window sampling and (3) the circular estimator method.

summarizes the evaluation of fracture network properties using these sampling methods and sampling method related biases (chapter 0). A general issue of fracture sampling is the minimum number of measurements required to adequately determine the characteristics of a fracture network. To evaluate the distribution of fracture lengths Priest (1993) suggests the measurement of 150 to 300 lengths, of which a minimum of 50 % should have at least one end visible. Bonnet et al. (2001) suggest that a minimum of 200 fracture lengths are required to define the exponent of a power-law length distribution. A study by Zeeb et al. (2013) presents the required minimum number of measurements for the individual sampling methods (Table 3). However, these numbers are not universally applicable. For example, to characterize fracture networks with strong spatial anisotropies, such as fracture clustering, intersecting fractures, complicated sampling area geometry (e. g. erosion features, vegetation or debris), and considerably more fracture lengths should be measured.

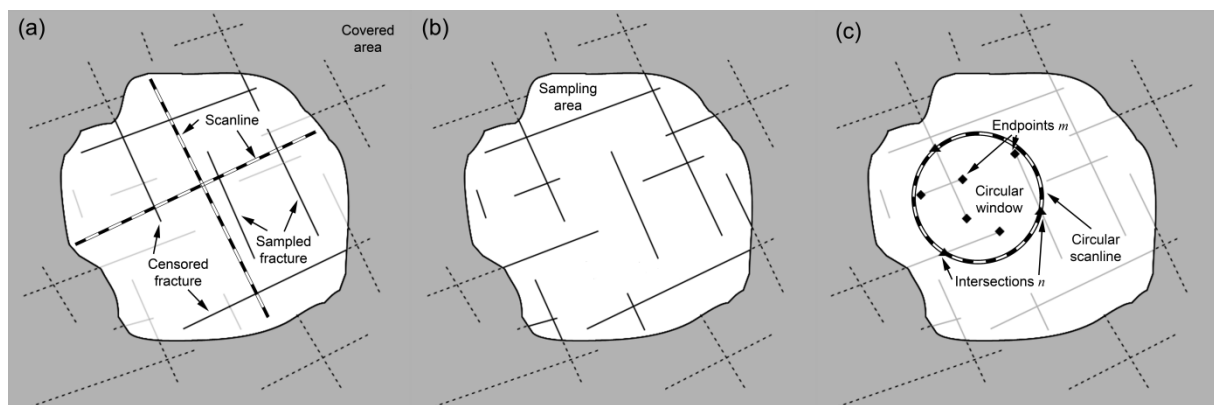


Fig. 5. (a) Scanline sampling, (b) window sampling, and (c) circular estimator method (modified from Rohrbaugh et al., 2002). Solid black lines indicate sampled fractures, light gray lines indicate non-sampled fractures and dashed lines non-observable (censored) parts of fractures (Zeeb et al., 2013).

Table 3. Summary of sampling method related fracture network properties and sampling biases for the scanline sampling, window sampling and circular estimator methods. The latter is based on Rohrbaugh et al. (2002). The minimum number of measurements are based on Zeeb et al. (2013) (modified from Zeeb et al., 2013).

Property		Definition	SLS	WS	CE
Density (ρ)	Areal ($P20$)	Number of fractures per unit area [m^{-2}]	-	$\rho_{WS} = \frac{N}{A}$	$\rho_{CE} = \frac{m}{2\pi r^2}$
	Volumetric ($P30$)	Number of fractures per unit volume [m^{-3}]	-	-	-
Intensity (I)	Linear ($P10$)	Number of fractures per unit length [m^{-1}]	$I_{SLS} = \frac{N}{L}$	-	-
	Areal ($P21$)	Fracture length per unit area [m m^{-2}]	-	$I_{WS} = \frac{\sum l}{A}$	$I_{CE} = \frac{n}{4r}$
	Volumetric ($P32$)	Fracture area per unit volume [m m^{-2}]	-	-	-
Spacing (S)	Linear	Spacing between fractures [m]	$S = 1/I_{SLS}$	-	-
Mean length (l_m)	Linear	Mean fracture length [m]	$l_{m;SLS} = \frac{\sum l}{N}$	$l_{m;WS} = \frac{\sum l}{N}$	$l_{m;CE} = \frac{\pi r n}{2 m}$
Length distribution	1D	Fractures intersecting with a scanline	yes	-	-
	2D	Fractures intersecting with a sampling area	-	yes	-
Orientation	2D	Orientation of a fracture on a sampling plane	yes	yes	-
	3D	Orientation of a fracture in a sampling volume	(yes) ^{a, b}	(yes) ^b	-
Sampling Bias		Orientation	yes	yes	-
		Truncation	yes	yes	-
		Size	yes	-	-
		Censoring	yes	yes	-
Minimum number of measurements			225	110	860 ^c

N is the total number of sampled fractures, L is the scanline length, A is the sampling area, r is the radius of the circular scanline, l is the fracture length, n and m are the number of intersections with a circular scanline and the number of endpoints in a circular window enclosed by the circular scanline.

^a Borehole: possible for oriented well cores and image logs.

^b Outcrop: possible for 3D outcrop settings.

^c Number of fractures contained in a sampling area.

4.1 Scanline sampling method

Scanline sampling (Fig. 5a) allows quick measurement of fracture properties from borehole data (e. g. well cores and image logs) or outcropping subsurface analogues (e. g. Priest and Hudson, 1981; Priest, 1993). A scanline is placed on the rock face or well core and the properties of fractures intersecting this scanline are measured. The method provides 1D stochastic properties of fracture networks (Table 3), such as linear fracture intensity (often also referred to as fracture frequency) or fracture spacing.

Scanline sampling is affected by: (1) orientation bias, (2) truncation bias, (3) censoring bias and (4) size bias.

Fracture density cannot be calculated directly from scanline measurements. Several equations and assumptions are required to calculate an areal fracture density based on the data of scanline surveys (Zeeb et al., 2013). Areal fracture intensity can be calculated from the product of fracture mean length and areal fracture density:

$$I = l_m \cdot \rho \quad \text{Eq. 9}$$

It is necessary to translate the linear fracture intensity calculated from scanline measurements into an areal fracture intensity. Provided that the scanline is perfectly parallel to the normal of a fracture set following relationship is found:

$$P10 = P21 = P32 \quad \text{Eq. 10}$$

Assuming that the fracture trace lengths are power-law distributed Eq. 8 can be applied to calculate a size bias independent fracture mean length. Combination and rearrangement of Eq. 8, Eq. 9 and Eq. 10 allows the calculation of an areal fracture density based on scanline measurements:

$$\rho = \frac{P10}{l_m} = \frac{P10 \cdot E_{1D}}{(E_{1D} + 1) \cdot l_0} \quad \text{Eq. 11}$$

4.2 Window sampling method

Window sampling (Fig. 5b) is used to measure the properties of all fractures present within a sampling window (Pahl, 1981; Wu and Pollard, 1995), and allows the calculation of 2D stochastic properties of fracture networks (Table 3). The method is typically applied to characterize fracture networks at outcropping subsurface analogues (e. g. Priest, 1993) or remote sensing data from satellite images or aerial photographs (e. g. Koike et al., 1995; Holland et al., 2009a; Zeeb et al., 2010). Three types of sampling bias affect window sampling: (1) orientation, (2) truncation and (3) censoring biases.

4.3 Circular estimator method

The circular estimator method, which is also referred to as the circular scanline and window method, uses a combination of circular scanlines and windows (Mauldon et al., 2001; Fig. 5c). The circular estimator method uses statistical models instead of measuring fracture properties (e. g. orientation or length) directly (Mauldon et al., 2001). A circular scanline is placed on a rock face and (1) the number of intersections n between this scanline and fractures, and (2) the number of fracture endpoints m inside the circular window formed by this scanline, are counted. Based on the n - and m -counts the areal fracture density, intensity and mean length are calculated (Table 3). The guideline for the circular estimator method suggests the application of at least ten circular scanlines to a sampling area, with each scanline having m -counts higher than 30 (Rohrbaugh et al., 2002). As a maximum likelihood estimator (Lyman, 2003), the method is not subject to sampling biases.

5 Modeling of fracture networks

Fracture networks in rock masses are often modeled using the discrete fracture network (DFN) approach, in which each fracture is represented as a discrete element (e. g. Blum et al., 2005; FracMan7, 2012; DFN_Lab, 2024). DFN models can be generated either deterministically, stochastically or geomechanically grown (Lei et al. 2017).

A **deterministic DFN** is the exact copy of a natural fracture network. This modeling approach is typically chosen for networks, which do not provide enough measurements for a statistical analysis (e. g. Zeeb et al., 2010). The results obtained from a deterministic model apply only to the studied fracture network.

A **stochastic DFN** is based on the statistical properties of a natural fracture network. The properties required to generate a stochastic DFN depends on the used software tool.

A **geomechanically grown DFN** is obtained by mimic the fracture generation process based on fracture mechanics. The generation process starts with assuming a microcrack distribution inside the considered rock mass. Based on applied boundary conditions and corresponding stress evolution crack propagation starts whenever critical stress intensity factors are reached at the crack tips. Ongoing crack propagation and interaction leads to the generation of complex fracture pattern (networks).

Table 4. Comparison of different approaches to generate DFN's (Lei et al., 2017)

Numerical models	Key inputs	Strengths	Limitations
Geological DFNs	Analogue mapping, borehole imaging, aerial photographs, LIDAR scan or seismic survey	(i) Preservation of geological realisms. (ii) Deterministic description of a fracture system.	(i) Limited feasibility for application to deep rocks. (ii) Difficulty in building 3D structures. (iii) Constraints from measurement scale and resolution.
Stochastic DFNs	Statistical data of fracture lengths, orientations, locations, shapes and their correlations	(i) Simplicity and convenience. (ii) Efficient generation. (iii) Applicability for both 2D and 3D. (iv) Applicability for various scales.	(i) Oversimplification of fracture geometries and topologies. (ii) Uncertainties in statistical parameters. (iii) Requirement of multiple realisations. (iv) Negligence of physical processes.
Geomechanical DFNs	Palaeostress conditions, rock and fracture mechanical properties	(i) Linking geometry with physical mechanisms. (ii) Correlation between different fracture attributes.	(i) Uncertainties in input properties and tectonic conditions. (ii) Large computational time. (iii) Negligence of hydrological, thermal and chemical processes.

DFN's can be implemented via different approaches in different numerical codes based on different techniques. Most popular are smeared approaches with classical continuum mechanical techniques like FEM/XFEM or FDM, particle or discrete element based approaches or hybrid continuum/discontinuum based ones (see Table 5).

In the current manuscript a 2D-DFN is generated using the non-commercial software tool FracFrac (Blum et al., 2005) and a 3D-DFN using the commercial software tool FracMan (FracMan7, 2012).

Table 5. Advantages and disadvantages of different approaches to simulate with DFN's (Lei et al., 2017)

Numerical models	Key inputs	Strengths	Limitations
Continuum models	Equivalent material properties	(i) Simplicity of geometries. (ii) Efficient calculation. (iii) Suitability for large-scale industrial applications.	(i) No consideration of fracture interaction, block displacement/interlocking/rotation. (ii) Complexity in deriving equivalent material parameters and constitutive laws. (iii) Valid only if an REV exists.
Block-type & particle-based discrete models	Material properties for both fractures and rocks, damping coefficient, bonding strengths	(i) Explicit integration of DFNs. (ii) Simple particle/grain bonding logic. (iii) Integrated constitutive laws for rocks/fractures. (iv) Capturing the interaction of multiple fractures.	(i) Limited data on joint stiffness parameters. (ii) Calibration of input particle bonding properties. (iii) No fracture mechanics principle. (iv) Large computational time.
Hybrid FEMDEM models	Material properties for both fractures and rocks, fracture energy release rate, damping coefficient	(i) Explicit integration of DFNs. (ii) Fracture propagation is based on both the strength criterion and fracture mechanics principles. (iii) Integrated constitutive laws for rocks/fractures. (iv) Capturing the interaction of multiple fractures.	(i) Limited data on joint stiffness parameters. (ii) Calibration of fracture energy release rates. (iii) Large computational time.

FracFrac (Blum et al., 2005) was developed using Visual Basic for Applications in Microsoft Excel™ and allows the generation of 2D-DFN. To generate a DFN fractures need to be grouped into sets, with each set being defined by (1) the average fracture strike, (2) the fracture length distribution, and (3) the fracture density. Based on the input fracture density, fracture centers are placed in a generation region applying a random Poisson distribution model (Blum et al., 2005). A fracture length with an orientation equal to the input average orientation is assigned to each center. The probability of a fracture length to occur in a fracture length population is described by the cumulative distribution of fracture lengths. Similar to FracFrac in FracMan fractures need to be grouped in sets, with each set being defined by (1) the average fracture orientation (dip and dip direction) and orientation distribution, (2) the fracture size distribution, (3) the fracture shape, and (4) the fracture intensity. The DFNs consist of two fracture sets with constant orientations. In 2D the average fracture strike is 30° for set 1 and 110° for set 2. For the 3D-DFN the dip and dip directions are 45° and 120° for set 1, and respectively 80° and 20° for set 2.

FracFrac and FracMan allow a variety of functions to describe the distribution of fracture sizes. However, power-law distributions are mostly used to describe the distribution of fracture sizes (chapter 2.2.4). To constrain the range of fracture lengths in a DFN it is necessary to define a lower cut-off. Latter is commonly related to a specific case study, the scale of observation, or truncation bias (chapter 3.2.2). The cumulative distribution of fracture lengths for a truncated power-law is given by (e. g. Blum et al., 2005; Riley 2005):

$$f(l) = 1 - \left(\frac{l}{l_0} \right)^{-E} \quad \text{Eq. 12}$$

where l is the fracture length, l_0 is the lower cut-off and E the exponent of the power-law function. Fig. 6a shows the cumulative distribution of fracture lengths for a truncated power-law with a lower cut-off of 1 m and an exponent of 2. The power-law exponent of the 3D size distribution is calculated using Eq. 5 and the shape of the fractures is assumed to be polygonal (Fig. 7b).

FracFrac generates DFN based on the areal fracture density $P20$ of each set, which were assumed to be 0.3 m⁻² for set 1 and 0.7 m⁻² for set 2. For the generation of DFN

using FracMan volumetric fracture intensities $P32$ are required. The areal fracture intensity can be expressed as the product of the areal fracture density and the fracture mean length (Eq. 9). Latter can be calculated from Eq. 7 and is 2 for the above described truncated power-law distribution. Applying Eq. 9 and Eq. 10 we get a volumetric fracture intensity of $0.6 \text{ m}^2 \text{ m}^{-3}$ for fracture set 1 and $1.4 \text{ m}^2 \text{ m}^{-3}$ for set 2. The 2D-DFN generated by FracFrac is shown in Fig. 6b and the 3D-DFN in Fig. 7.

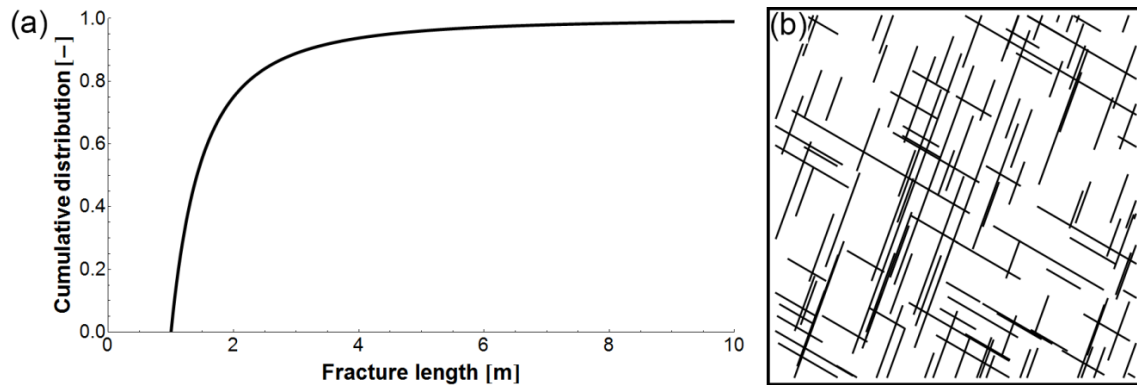


Fig. 6. (a) Plot of fracture lengths against their cumulative distribution for a truncated power-law function (Eq. 12) with a lower cut-off l_0 of 1m and an exponent E_{2D} of 2. (b) Ten by ten meter window of a 2D-DFN generated using the non-commercial software tool FracFrac (Blum et al., 2005). The fracture network consists of two sets with constant fracture strikes of 30° and 110° and fracture densities of 0.3 m^{-2} and 0.7 m^{-2} .

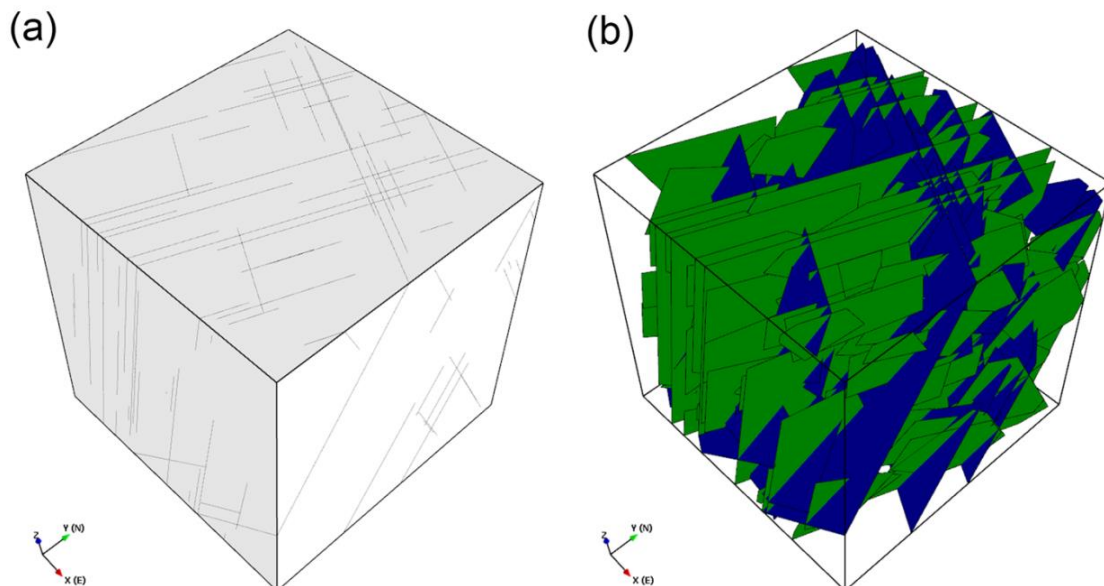


Fig. 7. 3D-DFN generated using the commercial software tool FracMan (FracMan7, 2012). The fracture network consists of two sets similar to those of the 2D-DFN shown in Fig. 6, with dip and dip directions of 45° and 120° for set 1, and respectively 80° and 20° for set 2. Application of equations Eq. 7, Eq. 9 and Eq. 10 allow the calculation of volumetric fracture intensities, which are $0.6 \text{ m}^2 \text{ m}^{-3}$ for set 1 and $1.4 \text{ m}^2 \text{ m}^{-3}$ for set 2. A polygonal fracture shape is assumed. (a) Fracture traces on the surface of the cube with an edge length of ten meters. (b) Fracture planes inside the cube with fracture set 1 marked in blue and set 2 marked in green.

6 Fluid transport simulations

Various techniques exist for the simulation of fluid transport in fractured media (e. g. Neumann, 2005). The simulation of fluid transport through a single fracture encompass methods to calculate (1) the spatial distribution of fluid flow characteristics in a fracture (e. g. lattice Boltzman methods), and (2) the hydraulic properties of an entire fracture (e. g. cubic law assumption) (e. g. Schwarz & Enzmann, 2013). The latter approach is more time efficient and therefore commonly used to simulate the fluid transport through a DFN. In DFN models each fracture is individually represented with its geometric properties (i.e. fracture length and aperture), which are translated into equivalent hydraulic properties (i.e. permeability or hydraulic conductivity). The fluid transport through a DFN depends on the geometric and hydraulic properties of the fracture network (e. g. Lee and Farmer, 1993) and models are typically treated in a stochastic framework (Berkowitz, 2002), meaning that multiple realizations of DFNs are studied using Monte Carlo analysis (e. g. Blum et al., 2005). Based on the results of such an analysis a 2D or 3D hydraulic conductivity tensor is calculated. Such a tensor can be used for the upscaling of the hydraulic properties of a meter-scale DFN to simulate the fluid transport on reservoir scale (km-scale) (e. g. Blum et al., 2009). The chapters below provide an introduction to (1) the simulation of fluid transport through a single fracture and (2) the simulation of fluid transport through a DFN as well as the concepts related to the subsequent upscaling of the hydraulic properties.

6.1 Fluid transport through a single fracture

6.1.1 Spatial distribution of fluid flow

Fractures in rocks exhibit asperities and therefore have rough surfaces. Even small in-plane shear movements result in a displacement of the fracture surfaces and a high spatial variation of fracture apertures (chapter 2.1.2; Fig. 2). Fluid transport is channeled towards open interconnected cavities, causing large spatial variations of fluid flow velocities within a single fracture. The spatial distribution of fluid flow characteristics in a single fracture is commonly determined by the numerical solution of the Navier-Stokes equation, e. g. by lattice Boltzmann methods (LBM) (e. g. Schwarz & Enzmann, 2013). An example for a numerical simulation of fluid transport in a rough fracture using the commercial software GeoDict (e. g. Khan et al., 2011) is presented in Fig. 8. The image shows the 3D fluid velocity distribution in a rough fracture. A typical application of such models is the simulation of mineral solution/precipitation, which is controlled by the amount of mineral nutrients transported by the fluid. In Fig. 8 mineral solution/precipitation would be highest in areas with high fluid velocities (red colored regions). Fluid velocities change over time as a result of the solution/precipitation process. The computation times required to run such simulations is a major drawback of this approach and simulations encompass therefore only small fractures or parts of fractures.

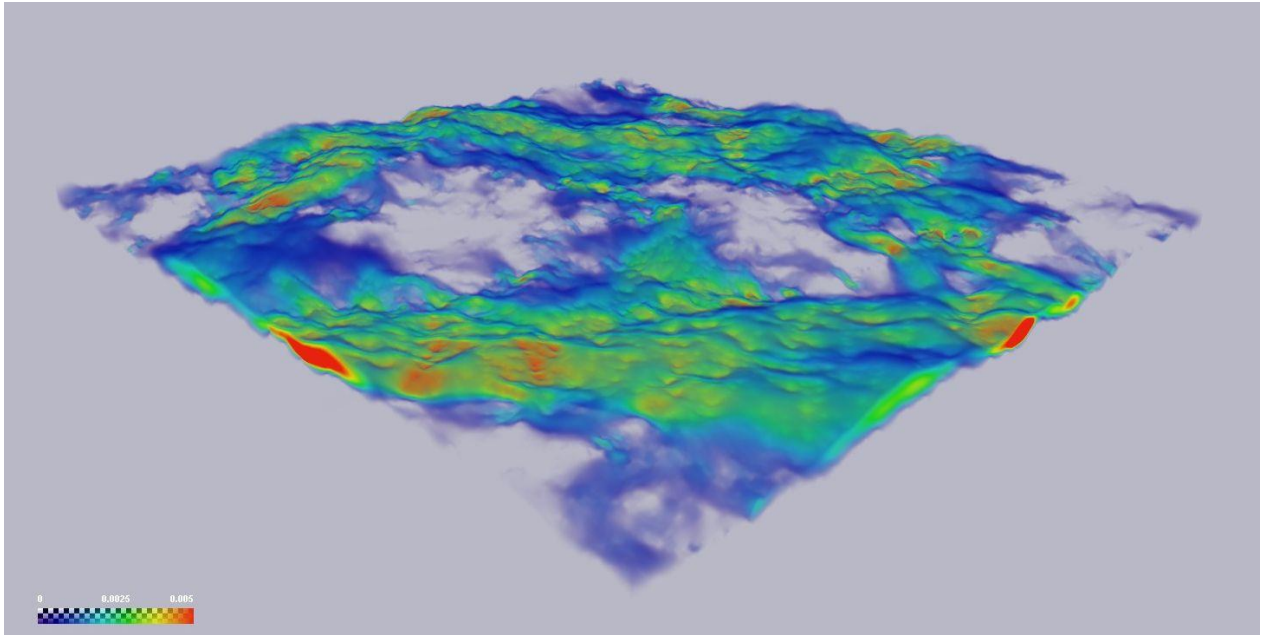


Fig. 8. Velocity field for the fluid transported through a rough fracture. Shown is the fracture void. The color code indicates the fluid velocity, with the highest velocities represented in red. Uncolored regions indicate areas where fracture surfaces touch, thereby forming rock bridges.

6.1.2 Cubic law assumption

Another more common approach to calculate the fluid transport through single fractures and fracture networks is the cubic law assumption, which is also referred to as parallel plate theory (Snow, 1965). In this approach fractures are treated as two parallel smooth plates with laminar fluid flow in between. The cubic law assumption is based on Darcy's law and the fluid flux Q through a single fracture is given by (Snow, 1965; Louis, 1967):

$$Q = \frac{\rho g a_h^3}{12\mu} \nabla h \quad \text{Eq. 13}$$

where ρ is the fluid density, g is the gravitational acceleration, a_h is the hydraulic aperture and ∇h is hydraulic gradient. The permeability K of a single fracture is:

$$K = \frac{a_h^2}{12} \quad \text{Eq. 14}$$

and the hydraulic conductivity k is:

$$k = \frac{\rho g K}{\mu} = \frac{\rho g a_h^2}{12\mu} \quad \text{Eq. 15}$$

The cubic law assumption is only valid for low Reynolds numbers. The Reynolds number Re is dimensionless and describes whether flow conditions are laminar (low Re), transitional, or turbulent (high Re). The Reynolds number Re is given by:

$$Re = \frac{\rho v d}{\mu} \quad \text{Eq. 16}$$

where v is the fluid velocity, d is the characteristic cross-sectional dimension and μ is the fluid viscosity. The critical Reynolds number Re_{cr} describes the transition from laminar to turbulent flow and ranges for rock joints between 2300 (Louis, 1974) and 100 (Iwai, 1976). A recent experimental study by Zhang & Nemcik (2013) showed that the critical Reynolds number is lower for displaced fracture surfaces. However, proving laminar flow for individual fractures is impractical and requires detailed knowledge about fracture and hydraulic properties. Moreover, experimental studies (e. g. Witherspoon et al., 1980) proved the validity of the cubic law assumption for the fluid transport in rough fractures.

6.2 Fluid transport through a fracture network

This chapter provides an introduction to the simulation of fluid transport through a 2D-DFN applying the cubic law assumption. Moreover, the basic concepts related to the upscaling of hydraulic properties are described. The presented methodology is based on Blum et al. (2005) and equivalent approaches are applicable to simulations of fluid transport through 3D-DFN (FracMan7, 2012).

6.2.1 Hydraulic properties of a DFN

The permeability (Eq. 14) and the hydraulic conductivity (Eq. 15) of a single fracture are functions of hydraulic fracture aperture, whereas the fluid transport through a network of interconnected fractures is more complex and is typically evaluated using numerical simulations. Blum et al. (2005) simulated fluid transport assuming Darcian flow across the DFN and applied the cubic law assumption to calculate the fluid flux through the individual fractures. A typical aim of such fluid transport simulations is the evaluation of a hydraulic tensor, which describes the directional anisotropy of hydraulic properties (hydraulic conductivity or permeability).

To solve the cubic law equation (Eq. 13) a hydraulic gradient needs to be applied. This gradient is the result of the difference in hydraulic heads or pore pressures between two points, for example the two endpoints of a fracture. Gradients in fracture networks are commonly unknown or difficult to measure. However, fluid flow is often forced through the fracture networks in hydrocarbon reservoirs, geothermal systems or fractured rock aquifers. Therefore, Blum et al. (2005) applied a gradient of one to evaluate the hydraulic conductivity of a DFN. The directional dependency of the hydraulic properties is evaluated by rotating this hydraulic gradient in several steps until the gradients cover a total of 180° (Fig. 9a). For each step the flow through the DFN is simulated and the fluid fluxes in x-direction (q_x) and y-direction (q_y) are calculated. These fluid fluxes are used to calculate the hydraulic conductivity components in x-, xy-, and y-direction (Jackson et al., 2000; Blum et al., 2005):

$$\begin{bmatrix} q_x \\ q_y \end{bmatrix} = \begin{bmatrix} k_{xx} & k_{xy} \\ k_{yx} & k_{yy} \end{bmatrix} \begin{bmatrix} \delta h / \delta x \\ \delta h / \delta y \end{bmatrix} \quad \text{Eq. 17}$$

where k_{xx} , k_{xy} and k_{yy} are the components of the hydraulic conductivity tensor in x-direction, xy-direction and y-direction, and $\delta h / \delta x$ and $\delta h / \delta y$ are the hydraulic head gradients in x- and y-direction. The hydraulic conductivity components need to be independent from the orientation of the hydraulic gradient. For a gradient of $\nabla h = 1$ the rotated gradients are:

$$\frac{\delta h}{\delta x} = \cos \phi \quad \text{Eq. 18}$$

$$\frac{\delta h}{\delta y} = \sin \phi \quad \text{Eq. 19}$$

where ϕ is the angle of the applied gradient. The minimum (k_{min}) and maximum (k_{max}) hydraulic conductivities as well as the orientation of the maximum hydraulic conductivity ϕ_{max} can be calculated by:

$$k_{max} = \frac{k_{xx} + k_{yy} + \sqrt{(k_{xx} + k_{yy})^2 - 4(k_{xx}k_{yy} - k_{xy}^2)}}{2} \quad \text{Eq. 20}$$

$$k_{min} = \frac{k_{xx} + k_{yy} - \sqrt{(k_{xx} + k_{yy})^2 - 4(k_{xx}k_{yy} - k_{xy}^2)}}{2} \quad \text{Eq. 21}$$

$$\phi_{max} = \tan^{-1} \left(\frac{k_{max} - k_{xx}}{k_{xy}} \right) \quad \text{Eq. 22}$$

Fig. 9b shows the tensor representing the directional dependent hydraulic conductivities for the DFN in Fig. 9a.

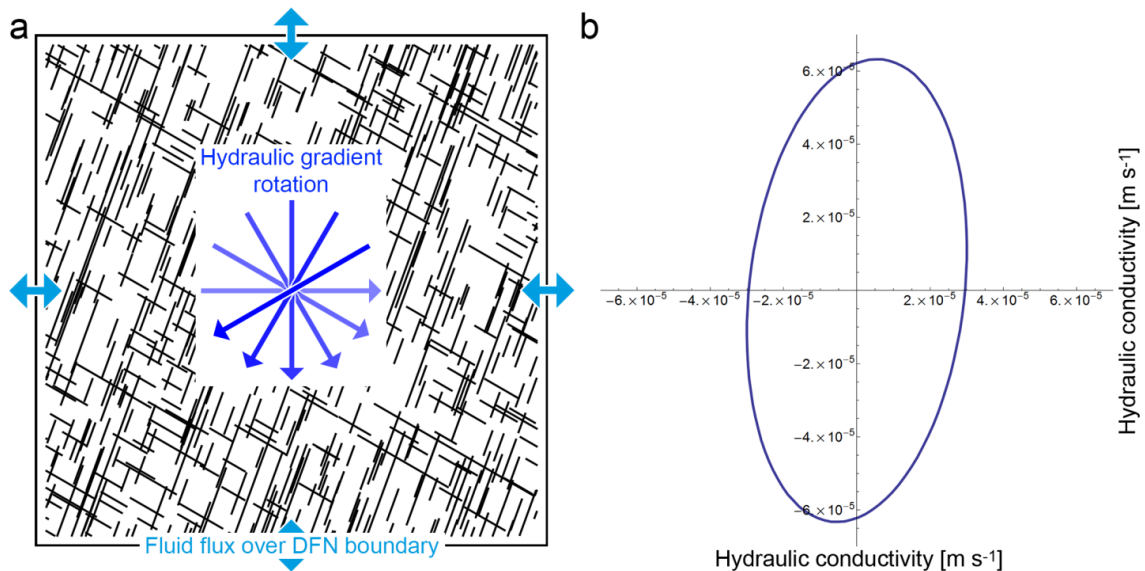


Fig. 9. (a) DFN with an edge length of 25 m. The dark-blue arrows indicate the rotation of the hydraulic gradient in steps of 30° until the gradients cover a total of 180°. The light-blue arrows indicate the fluid flux over the DFN boundaries. (b) The hydraulic conductivity tensor of the DFN shown in (a).

6.2.2 Equivalent porous media

Hydraulic conductivity tensors as shown in Fig. 9b are used for the upscaling of the hydraulic properties obtained from DFN models. Such upscaled properties are typically used to parameterize large scale (km-scale) reservoir models, which are usually too large for the application of a discrete element method (DEM) like the DFN approach. Therefore, the Finite Element Method (FEM), in which geologic formations are treated as continuous porous media, is commonly applied to simulate fluid transport on reservoir scale. To parameterize the FEM model the hydraulic properties of a DFN are translated into an equivalent porous media (EPM). This means that a discontinuous volume of fractured rock is transformed into a continuous porous rock volume with (anisotropic) hydraulic conductivities equivalent to those of the DFN.

6.2.3 Representative elementary volume

Applying upscaled hydraulic conductivity tensors to parameterize a large-scale model requires the tensor to be representative of the modeled geologic formation. To assure that a tensor is representative it is necessary to define the representative elementary volume (REV) of a DFN (e. g. Blum et al., 2005). The REV is evaluated by generating DFNs of different size but constant stochastic properties. For each DFN the hydraulic conductivity tensor is calculated and the DFN size is plotted against, for example, the maximum hydraulic conductivity. If the size of the DFN is too small, the fluid transport is completely dominated by the geometric properties of a few large fractures. This causes a high variability of hydraulic conductivities calculated for DFNs with a size below the REV (Fig. 10). The minimum size above which DFNs exhibit similar hydraulic conductivity tensors is the REV. Fig. 10 shows a plot of the edge length against minimum and maximum hydraulic conductivity for quadratic DFNs. The hydraulic conductivities are almost constant for DFNs with an edge length of 25 m or more. This implies that all DFNs with an edge length of 25 m or more have a REV.

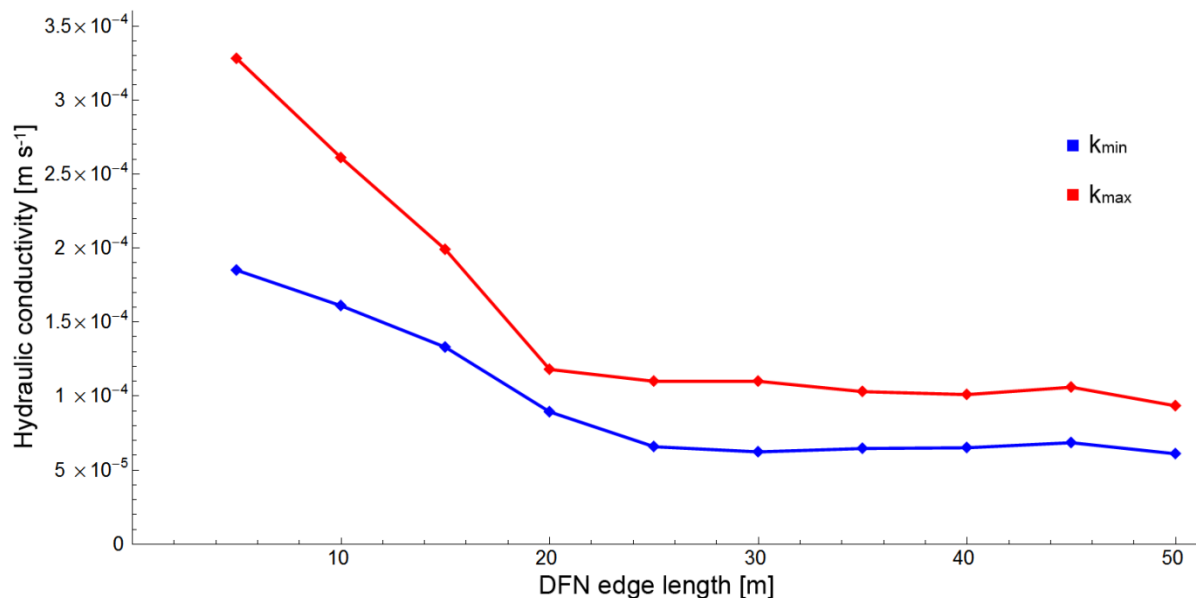


Fig. 10. Plot of DFN edge length against minimum (k_{min}) and maximum (k_{max}) hydraulic conductivity for quadratic fracture networks (chapter 5, Fig. 6b). The DFN have the same stochastic properties. All DFNs with an edge length of 25 m have a REV.

7 References

- Barthélémy, J.-F., M. L. E. Guiton, J.-M. Daniel, 2009. Estimates of fracture density and uncertainties from well data: *International Journal of Rock Mechanics and Mining Sciences*, v. 46, p. 590 – 603.
- Barton, N. R., Choubey, V., 1977. The shear strength of rock joints in theory and practice. *Rock Mechanics*, v. 10, p. 1 – 54.
- Barton, N., S. Bandis, 1980. Technical Note: Some Effects of Scale on the Shear Strength of Joints: *International Journal of Rock Mechanics, Mining Sciences & Geomechanical Abstracts*, v. 17, p. 69 – 73.
- Barton, N., S. Bandis, K. Bakhtar, 1985. Strength, Deformation and Conductivity Coupling of Rock Joints: *International Journal of Rock Mechanics, Mining Sciences & Geomechanical Abstracts*, v. 22, p. 121 – 140.
- Barton, N., E. F. de Quadros, 1997. Joint aperture and roughness in the prediction of flow and groutability of rock masses: *International Journal of Rock Mechanics and Mining Sciences*, v. 34.
- Belayneh, M. W., S. K. Matthäi, M. J. Blunt, and S. F. Rogers, 2009, Comparison of deterministic with stochastic fracture models in water-flooding numerical simulations: *AAPG Bulletin*, v. 93, p. 1633 – 1648.
- Berkowitz, B., 2002. Characterizing flow and transport in fractured geological media: A review. *Advances in Water Resources*, v. 25, p. 861 – 884.
- Blum, P., R. Mackay, M. S. Riley, J. L. Knight, 2005. Performance assessment of a nuclear waste repository: Upscaling coupled hydro-mechanical properties for far-field transport analysis: *Journal of Rock Mechanics and Mining Sciences*, v. 42, p. 781 – 792.
- Blum, P., R. Mackay, M. S. Riley, 2009. Stochastic simulations of regional scale advective transport in fractured rock masses using block upscaled hydro-mechanical rock property data: *Journal of Hydrology*, v. 369, p. 318 – 325.
- Bonnet, E., O. Bour, N. E. Odling, P. Davy, I. Main, P. Cowie, B. Berkowitz, 2001. Scaling of fracture systems in geological media: *Reviews of Geophysics*, v. 39, p. 347 – 383.
- Bons, P. D., M. A. Elburg, E. Gomez-Rivas, 2012. A review of the formation of tectonic veins and their microstructures: *Journal of Structural Geology*, v. 43, p. 33 – 62.
- Cruden, D. M., 1977. Describing the size of discontinuities: *International Journal of Rock Mechanics and Mining Sciences Geomechanical Abstracts*, v. 14, p. 133 – 137.
- Darcel, C., O. Bour, P. Davy, 2003. Stereological analysis of fractal fracture networks: *Journal of Geophysical Research*, v. 108, p. 1 – 14.
- Dershowitz, W. S., 1984, Rock joint systems: Ph.D. dissertation, Massachusetts Institute of Technology, Cambridge, Massachusetts, 918 p.
- DFN_lab, 2024, <https://fractorylab.org/dfnlab-software/>
- Durham, W. B., B. P. Bonner, 1994. Self-propping and fluid flow in slightly offset joints at high effective pressures: *Journal of Geophysical Research*, v. 99, p. 9391 – 9399.
- Forte, E., M. Pipan, D. Casabianca, R. Di Cuia, A. Riva, 2012. Imaging and characterization of carbonate hydrocarbon reservoir analogue using GPR attributes: *Journal of Applied Geophysics*, v. 81, p. 76 – 87.
- FracMan7, 2012. Golder Associates Inc., <http://www.golder.com>
- Goel, R. K., Singh, B., 2011. *Engineering Rock Mass Classification*. Elsevier.
- Hatton, C. G., I. G. Main, P. G. Meredith, 1993. A comparison of seismic and structural measurements of fractal dimension during tensile subcritical crack growth: *Journal of Structural Geology*, v. 15, p. 1485 – 1495.
- Holland, M., J. L. Urai, P. Muecher, E. J. M. Willemsse, 2009a. Evolution of fractures in a highly dynamic thermal, hydraulic, and mechanical system - (I) Field observations in Mesozoic Carbonates, Jabal Shams, Oman Mountains: *GeoArabia*, v. 14, p. 57 – 110.

- Hudson, J. A., and S. D. Priest, 1983, Discontinuity frequency in rock masses: *International Journal of Rock Mechanics and Mining Sciences and Geomechanical Abstracts*, v. 20, p. 73 – 89.
- Iwai, K., 1976. *Fundamental studies of fluid flow through a single fracture*: PhD Thesis, University of California, Berkeley, 208pp.
- Jackson, C. P., Hoch, A. R., Todman, S., 2000. Self-consistency of a heterogeneous continuum porous medium representation of fractured media: *Water Resources Research*, v. 36, p. 189 – 202.
- Jeanne, P., Y. Guglielmi, F. Cappa, 2012. Multiscale seismic signature of a small fault zone in a carbonate reservoir: Relationships between Vp imaging, fault zone architecture and cohesion: *Tectonophysics*, v. 554 – 557, p. 185 – 201.
- Khan, F., F. Enzmann, M. Kersten, A. Wiegmann, K. Steiner 2011. 3D simulation of the permeability tensor in a soil aggregate on basis of nanotomographic imaging and LBE solver: *Journal of Soils and Sediments*, v. 12, p. 86 – 96.
- Koike, K., S. Nagano, M. Ohmi, 1995. Lineament analysis of satellite images using a segment tracing algorithm (STA): *Computers and Geosciences*, v. 21, p. 1091 – 1104.
- Kulatilake, P. H. S. W., T. H. Wu, 1984. The density of discontinuity traces in sampling windows (technical note): *International Journal of Rock Mechanics and Mining Sciences and Geomechanical Abstracts*, v. 21, p. 345 – 347.
- Lacazette, A., 1991. A new stereographic technique for the reduction of scanline survey data of geologic features: *Computers and Geosciences*, v. 17, p. 445 – 463.
- LaPointe, P. R., 2002. Derivation of parent population statistics from trace length measurements of fractal populations: *International Journal of Rock Mechanics and Mining Sciences*, v. 39, p. 381 – 388.
- Laubach, S. E., 2003. Practical approaches to identifying sealed and open fractures: *AAPG Bulletin*, v. 87, p. 561 – 579.
- Laubach, S. E., M. E. Ward, 2006. Diagenesis in porosity evolution of opening-mode fractures, Middle Triassic to Lower Jurassic La Boca Formation, NE Mexico: *Tectonophysics*, v. 419, p. 75 – 97.
- Lee, C.-H., I. Farmer, 1993. *Fluid flow in discontinuous rock*: London, Chapman & Hall, 169 p.
- Lei, Q. et al., 2017. The use of discrete fracture networks for modelling coupled geomechanical and hydrological behavior of fractured rocks, *Computers and Geotechnics*, 85, 151-176
- Louis, C., 1967. *Strömungsvorgänge in klüftigen Medien und ihr Wirkung auf die Standsicherheit von Bauwerken und Böschungen im Fels* [Flow phenomena in fractured systems and their contribution to structural integrity of buildings and slopes at rock]. PhD Thesis, Technical University Karlsruhe, Germany.
- Louis, C., 1974. Introduction à l'hydraulique des roches: *Bulletin BRGM 2ième série, Section III*, v. 4, p. 283 – 356.
- Mauldon, M., W. M. Dunne, M. B. Rohrbaugh, Jr., 2001. Circular scanlines and circular windows: new tools for characterizing the geometry of fracture traces: *Journal of Structural Geology*, v. 23, p. 247 – 258.
- Narr, W., 1996. Estimating average fracture spacing in subsurface rock: *AAPG Bulletin*, v. 80, p. 1565 – 1586.
- Neuman, S. P., 2005. Trends, prospects and challenges in quantifying flow and transport through fractured rocks: *Hydrogeology Journal*, v. 13, p. 124 – 147.
- Neuman, S. P., 2008. Multiscale relationship between fracture length, aperture, density and permeability: *Geophysical Research Letters*, v. 35, p. 1 – 6.
- Nirex, 1997b. Evaluation of heterogeneity and scaling of fractures in the Borrowdale Volcanic Group in the Sellafield area: Nirex Report SA/97/028, Harwell.

- Odling, N. E., 1997. Scaling and connectivity of joint systems in sandstones from western Norway: *Journal of Structural Geology*, v. 19, p. 1257 – 1271.
- Olson, J. E., 2003. Sublinear scaling of fracture aperture versus length: An exception or the rule? *Journal of Geophysical Research (American Geophysical Union)*, v. 108, no. B9, 2413.
- Olson, J. E., S. E. Laubach, R. H. Lander, 2009. Natural fracture characterization in tight gas sandstones: Integration mechanics and diagenesis: *AAPG Bulletin*, v. 93, p. 1535 – 1549.
- Olson, J. E., R. A. Schultz, 2011. Comment on " A note on the scaling relations for opening mode fractures in rock" by C.H. Schultz: *Journal of Structural Geology*, v. 33, p. 1523 – 1524.
- Ortega, O. J., R. A. Marrett, 2000. Prediction of macrofracture properties using microfracture information, Mesaverde Group sandstones, San Juan basin, New Mexico: *Journal of Structural Geology*, v. 22, p. 571 – 588.
- Pahl, P. J., 1981. Estimating the mean length of discontinuity traces: *International Journal of Rock Mechanics and Mining Sciences & Geomechanics Abstracts*, v. 18, p. 221 – 228.
- Pérez-Claros, J. A., P. Palmqvist, F. Olóriz, 2002. First and second orders of suture complexity in ammonites: A new methodological approach using fractal analysis: *Mathematical Geology*, v. 34, p. 323 – 343.
- Philip, Z. G., J. W. Jennings Jr., J. E. Olson, S. E. Laubach, J. Holder, 2005. Modelling coupled fracture-matrix fluid flow in geomechanically simulated fracture networks: *Society of Petroleum Engineers*.
- Pickering, G., J. M. Bull, D. J. Sanderson, 1995. Sampling power-law distributions: *Tectonophysics*, v. 248, p. 1 – 20.
- Pollard, D. D., P. Segall, 1987. Theoretical displacements and stresses near fractures in rocks: with applications to faults, joints, dikes and solution surfaces: In: Atkinson, B.K. (Ed.), *Fracture Mechanics of Rock*. Academic Press, London, p. 277 – 348.
- Priest, S. D., J. A. Hudson, 1981. Estimation of discontinuity spacing and trace length using scanline surveys: *International Journal of Rock Mechanics and Mining Sciences & Geomechanics Abstracts*, v. 18, p. 183 – 197.
- Priest, S. D., 1993. *Discontinuity analysis for rock engineering*. London, Chapman & Hall, 473 p.
- Priest, S. D., 2004. Determination of discontinuity size distributions from scanline data: *Rock Mechanics and Rock Engineering*, v. 37, p. 347 – 368.
- Renshaw, C. E., J. S. Dadakis, S. R. Brown, 2000. Measuring fracture apertures: A comparison of methods: *Geophysical Research Letters*, v. 27, p. 289 – 292.
- Riley, M. S., 2005. Fracture trace length and number distributions from fracture mapping: *Journal of Geophysical Research*, v. 110.
- Rohrbaugh, Jr., M. B., W. M. Dunne, M. Mauldon, 2002. Estimating fracture trace intensity, density and mean length using circular scanlines and windows: *AAPG Bulletin*, v. 86, p. 2089 – 2104.
- Roy, A., E. Perfect, W. M. Dunne, L. D. McKay, 2007. Fractal characterization of fracture networks: an improved box-counting technique: *Journal of Geophysical Research*, v. 112, B12201.
- Sausse, J., C. Dezayes, L. Dorbath, A. Genter, J. Place, 2010. 3D model of fracture zones at Soultz-sous-Forêts based on geological data, image logs, induced microseismicity and vertical seismic profiles: *Comptes Rendus Geoscience*, v. 342, p. 531 – 545.
- Scholz, C. H., 2002. *The Mechanics of Earthquakes and Faulting*: second ed. Cambridge University Press, Cambridge.
- Scholz, C. H., 2010. A note on the scaling relations for opening mode fractures in rock: *Journal of Structural Geology*, v. 32, p. 1485 – 1487.

- Schwarz, J.-O., F. Enzmann, 2013. Simulation of Fluid Flow on Fractures and Implications for Reactive Transport Simulations: *Transport in Porous Media*, v. 96, p. 501 – 525.
- Sellers, E. J., P. Klerck, 2000. Modelling of the effect of discontinuities on the extent of the fracture zone surrounding deep tunnels: *Tunnelling and Underground Space Technology*, v. 15, p. 463 – 469.
- Snow, D. T., 1965. A parallel plate model of fractured permeable media. PhD Thesis, University of California, Berkeley, USA.
- Sudha, K., B. Tezkan, M. Israil, J. Rai, 2011. Combined electrical and electromagnetic imaging of hot fluids within fractured rock in rugged Himalayan terrain: *Journal of Applied Geophysics*, v. 74, p. 205 – 214.
- Terzaghi, R. D., 1965, Sources of error in joint surveys: *Géotechnique*, v. 13, p. 287 – 304.
- Tóth, T. M., 2010. Determination of geometric parameters of fracture networks using 1D data: *Journal of Structural Geology*, v. 32, p. 1271 – 1278.
- Van der Pluijm, B. A., S. Marshak, 2004. *Earth Structure – An Introduction to Structural Geology and Tectonics (Second Edition)*. W. W. Norton & Company, New York, US.
- Witherspoon, P. A., Wang, J. S. Y., Iwai, K., Gale, J. E., 1980. Validity of cubic law for fluid flow in a deformable rock fracture: *Water Resources Research*, v. 16, p. 1016 – 1024.
- Wu, H., D. D. Pollard, 1995. An experimental study of the relationship between joint spacing and layer thickness: *Journal of Structural Geology*, v. 17, p. 887 – 905.
- Zeeb, C., D. Göckus, P. Bons, H. Al Ajmi, R. Rausch, P. Blum, 2010. Fracture flow modelling based on satellite images of the Wajid Sandstone, Saudi Arabia: *Hydrogeology Journal*, v. 18, p. 1699 – 1712.
- Zeeb, C., E. Gomez-Rivas, P. D. Bons, P. Blum, 2013. Evaluation of sampling methods for fracture network characterization using outcrops: *AAPG Bulletin*, v.97, p. 1545 – 1566.
- Zhang, L., H. H. Einstein, 1998. Estimating the mean trace length of rock discontinuities: *Rock Mechanics and Rock Engineering*, v. 31, p. 217 – 235.
- Zhang, Z., Nemcik, J., 2013. Fluid flow regimes and nonlinear flow characteristics in deformable rock fractures: *Journal of Hydrology*, v.477, p. 139 – 151.